Elaboration and luminescence properties of Laser Heated Pedestal Growth (LHPG) Sr3Al2O6-based fibers

Alberto José Fernández-Carrión, Julie Bourret, James Sharp, Mengchuan Xing, Jean-René Duclère, Maggy Colas, Julie Cornette, Pierre Carles, Cécile Genevois, François Brisset, et al.

Elaboration and luminescence properties of Laser Heated Pedestal Growth (LHPG) $Sr_3Al_2O_6$-based fibers

Alberto José Fernández-Carrión[1], Julie Bourret[1], James Sharp[2], Mengchuan Xing[2], Jean-René Duclère[1], Maggy Colas[1], Julie Cornette[1], Pierre Carles[1], Cécile Genevois[3], François Brisset[4], Sébastien Chenu[1], Mathieu Allix[3], Gaëlle Delaizir[1*]

[1]*Institut de Recherche sur les Céramiques (IRCER), UMR 7315 CNRS, Université de Limoges, Centre Européen de la Céramique, Limoges, France*

[2] *School of Engineering, James Watt Building, Glasgow University, Glasgow, UK*

[3]*Conditions Extrêmes et Matériaux : Haute Température et Irradiation (CEMHTI), UPR 3079 CNRS, Orléans, France*

[4]*Institut de Chimie Moléculaire et des Matériaux d'Orsay (ICMMO), UMR 8182 CNRS, Orsay, France*

*Corresponding author: gaelle.delaizir@unilim.fr

Abstract

The development of transparent optical fibers represents one of the biggest scientific challenges for a wide variety of modern technologies ranging from communication systems to medical applications. Here, transparent $Sr_3Al_2O_6$ crystalline fibers have been grown by the laser-heated pedestal growth (LHPG) technique and the effect of using unconventional glass or ceramic seed is discussed. These fibers exhibit a unique micro and nanostructure made of veins dispersed in a single orientated $Sr_3Al_2O_6$ crystalline matrix which has been thoroughly characterized by using electron backscatter diffraction (EBSD) and high-resolution transmission microscopy (HRTEM). The LHPG method also successfully produced optical fibers of 1 at% Er^{3+}-doped $Sr_3Al_2O_6$. Even when other impurity was detected, the emission spectrum of the fiber presented sharp Er^{3+} emission bands and long fluorescence lifetime values arising from the high crystalline structure perfection provided by the LHPG method.

1. INTRODUCTION

Despite the successful applications of silica-based glass optical fibers as sensors or fiber lasers, they are not competitive for applications requiring extreme environmental conditions such as high temperatures, radioactivity, corrosion or high energy fluences. Laser-heated pedestal growth (LHPG) and micro-pull-down techniques have been well studied and used with increasing success to prepare crystalline fibers that are thermally, mechanically and chemically more robust than glass fibers.[1-5] The former is basically a miniature floating-zone-like method where the heating element is replaced by a focused laser ring to generate the molten zone. This can achieve rather high temperatures, and thereby highly refractive compositions can be melted in. The LHPG technique also has the advantage of being a containerless method and thereby preventing contamination from the crucible, which is of utmost importance as high quality optical materials are pursued.

The LHPG technique has been employed to prepare several single crystal or polycrystalline optical fibers based on binary, ternary or even quaternary compounds.[6-12] Among them, aluminate based-compositions such as YAG or sapphire have proven high optical efficiency and are attractive for optical applications.[6-9, 13] Nevertheless, even when the usefulness of the LHPG technique has been proved, it has been scarcely explored so far. The main compositional requirement is the existence of a congruent crystallization from the molten state.

Highly transparent polycrystalline ceramic, based on $Sr_3Al_2O_6$ composition has been fabricated by full crystallization from the parent glass.[14] This compound was crystallized from a bulk-glass precursor prepared by the innovative aerodynamic levitation method and features optical transparency both in the visible and infrared (until 6 μm) spectral ranges. The authors attributed its high transparency to the high density (i.e. complete absence of porosity) and micrometer-scale grains with very thin grain boundaries, as well as its intrinsic cubic crystalline

structure (S.G. *Pa*-3) leading to optical isotropy (i.e. no birefringence is present). This composition is well adapted for laser applications as illustrated by the luminescence spectra of $Sr_3Al_2O_6$ ceramics doped with various rare-earth ions.[14, 15] The main drawback of the aerodynamic levitation method is the limited size of the samples, typically small beads of diameter ~3-5 mm.

Owing to the crystal structure features, chemical stability, and optical properties, the fabrication of an active $Sr_3Al_2O_6$ transparent ceramic fiber may be a significant breakthrough for laser-based technologies. Nevertheless, the optical transparency of this composition highly depends on the container employed during preparation. Indeed, Al Saghir *et al*. demonstrated that transparency cannot be attained by using the classic melt-quenching process using Pt/Rh crucibles owing to dark opaque materials being obtained.[16] This drawback may be overcome by using the LHPG method as it eliminates contamination problems arising from crucibles and furnace components.[2, 5]

In this work, we present a novel process to prepare the green-bodies (feed pedestals) by using a microextrusion machine to extrude the source rods for the growth of $Sr_3Al_2O_6$ and Er^{3+}-doped $Sr_3Al_2O_6$ crystalline fibers by the LHPG technique. In addition, we employed two different kinds of seeds: $Sr_3Al_2O_6$ glass and transparent ceramic seeds in place of the more commonly used crystallographic seed. A careful look at the structure, microstructure and the photoluminescence (PL) of Er-doped crystalline fibers is presented and compared to $Sr_3Al_2O_6$ glass and polycrystalline bulks. The high crystal perfection obtained results in very intense and better defined emission bands when compared with the polycrystalline material counterpart.

2 MATERIALS AND METHODS

2.1 Preparation of $Sr_3Al_2O_6$ source rods for LHPG experiment

Source rods were prepared by mixing Al_2O_3 (99.7%, Sigma-Aldrich) with 1 wt.% of dispersant in an agate mortar. Then, it was added the appropriate molar ratio of $SrCO_3$ (99.9%,

sigma Aldrich) and Er_2O_3 along with 40 % of the total weight of methyl cellulose as binder and 3 vol.% of glycerol as lubricant. The previous mixture was mixed in an agate mortar until producing a homogeneous paste which was introduced three times into a three rolls mill system to eliminate agglomerates. The resulting paste was extruded using homemade extrusion equipment through a Ø 1 mm stainless-steel die (Figure S1). The extruded green rods were air dried overnight and then used for drawing the fibers. The manual extrusion process led to shorter pedestals, with irregular shapes and superficial defects.

2.2 Preparation of $Sr_3Al_2O_6$ glass and transparent ceramic used as seed

The Er-doped $Sr_3Al_2O_6$ glasses were synthesized from high purity $SrCO_3$ (99.99%), Al_2O_3 (99.98%) and Er_2O_3 (1 at% Er^{3+} substitutes 1 at% Sr^{2+}) oxides using an aerodynamic levitator equipped with two CO_2 lasers. Er_2O_3 was calcined at 900 °C overnight. The starting materials were first weighed in stoichiometric amounts, mixed, and pressed into pellets. To elaborate a glass bead, a piece of the pellet was placed in the levitator system's conical nozzle and melted, at around 1800 °C, using the CO_2 lasers. The melt was levitated by an argon flow, and glass beads (1.5 mm in diameter) were obtained by quenching (realized by cutting off the two laser beams with a cooling rate of approximately 300°C/s). The corresponding transparent ceramic was obtained by congruent and full crystallization from the parent glass by a heat treatment at 840 °C for 5 h in an open-air tubular furnace.[14]

These $Sr_3Al_2O_6$ glasses and transparent ceramics were used as seeds by cutting the bulk materials into parallelepipeds with size 1 x 1 x 5 mm and used as a reference to compare the photoluminescence (PL) properties of the $Sr_3Al_2O_6$ fiber grown by the LHPG technique.

2.3 Fiber preparation

The fibers were obtained by an LHPG equipment. Micro-extruded rods were used as source materials and $Sr_3Al_2O_6$ glass or polycrystalline ceramic were used as seeds. The fibers

were grown at 0.14 mm/min and common incident CO_2 laser power of approximately 8 W was maintained during growth. Symmetrical heating of the melt was obtained using a standard reflaxicon arrangement. Fibers were grown 'open loop', i.e. without active diameter control. The low density of the source rods made fiber growth difficult to stabilise and hence the relatively slow pull rate of the fibers. The final fibers were approximately 800 μm in diameter with lengths ranging from 5 to 12 mm.

2.4 Characterizations

Electron backscatter diffraction (EBSD) maps were recorded on the $Sr_3Al_2O_6$ LHPG fibers using an OIM TSL/EDAX system mounted on a FEG-SEM (Zeiss SUPRA 55 VP) system in order to confirm the single or polycrystalline nature of our fibers.

Laboratory X-Ray Powder Diffraction (XRD) measurements were performed on crushed powder fibers using a Bragg-Brentano D8 Advance Bruker laboratory diffractometer (Cu Kα radiation) equipped with a lynxEye XE detector.

The nanostructure of the fiber was characterized by Transmission Electron Microscopy (TEM) micrographs, scanning transmission electron microscopy – high angle annular dark field (STEM-HAADF) imaging and EDS elemental analyses. These experiments were performed on a JEOL ARM 200F (JEOL Ltd.) Cold FEG TEM operating at 200kV, equipped with a double spherical aberration corrector and fitted with a JEOL SDD CENTURIO EDS system. STEM-HAADF imaging and STEM-EDS elemental maps were acquired with a 0.1nm probe size. The samples were prepared prior to (S)TEM observations by Focused Ion Beam (FIB, Zeiss Crossbeam 550).

Raman spectroscopy characterizations of the LHPG fiber were performed using an In Via Reflex Renishaw Raman spectrophotometer. The spectra were recorded using a x50 objective with 532 nm wavelength excitation and low power at the sample (3 mW) to avoid any damage. Raman maps have been recorded with high-resolution mode, using a 2400 grooves/mm

grating. An area of 58 x 66 μm^2 has been studied and maps have been reconstructed using principal component analysis (PCA) method on a collection of 1020 spectra. Data have been truncated between 668 and 810 cm^{-1} and the baseline subtracted. The first two components explain 96.7% of the data.

The microstructure of the LHPG fibers and the chemical compositions were observed and checked using scanning electron microscopy (EDS-SEM, JEOL IT 300 LV).

Room temperature Near InfraRed photoluminescence (PL) properties were measured using a Horiba-Jobin-Yvon Fluorolog 3 spectrofluorimeter, operated in reflective geometry. For the recorded emission spectra in the 1400-1650 nm range, the data step was fixed to 0.5 nm, with a 2.5 nm emission slit size which was found appropriate for comparing all the analyzed samples. For measuring the PL decay curves, an initial delay time of 0.2 ms was set. Data were then acquired with a time interval step of 0.2 ms, up to a final decay time of 50 ms. Lifetime values were extracted through a fitting procedure of the PL decay curves data, which employs either some single or double exponential decay function(s). Average lifetime values are finally calculated.

3 RESULTS AND DISCUSSION

3.1 Fiber structure

$Sr_3Al_2O_6$ fibers were successfully obtained from extruded source rods of glass or transparent ceramic used as seeds as shown in Figure 1, although the drawing process was easier when extruded transparent seed ceramic were employed. It should be stressed that the drawing of $Sr_3Al_2O_6$ fibers is highly dependent on the initial state of the pedestals. Initially, sintered square pedestals of ~1.5mm cross section were employed. Even when small fibers could be grown, their lengths were typically shorter than 9 mm (Figure S1) and the cross section of the fibers were difficult to keep constant. The effect of the pedestal shape was discussed by Reyes Ardila et al.[17] for the preparation of $SrTiO_3$ fibers by LHPG. They found that rod pedestals

prepared by extrusion were more suitable than squared-shape pedestals because the laser beam matches up better with the feed rod geometry. The authors also indicated some drawbacks arising from the extrusion process. Among them, lamination, surface and edge tearing. For this reason, we incorporated several steps when preparing the green bodies source rods. These include the addition of glycerol as lubricant, as well as agglomerate elimination through a three rolls mill system. Then, the green bodies were extruded by using 3D-ceramic technology which allows a constant pressure during the extrusion process, leading to perfectly straight pedestal and enhancing the final quality of the source rods. The as-prepared rods were dried in air, and further annealing treatments were avoided in order to limit furnace contamination, as well as the shrinkage of the pedestal which led to pucker them.

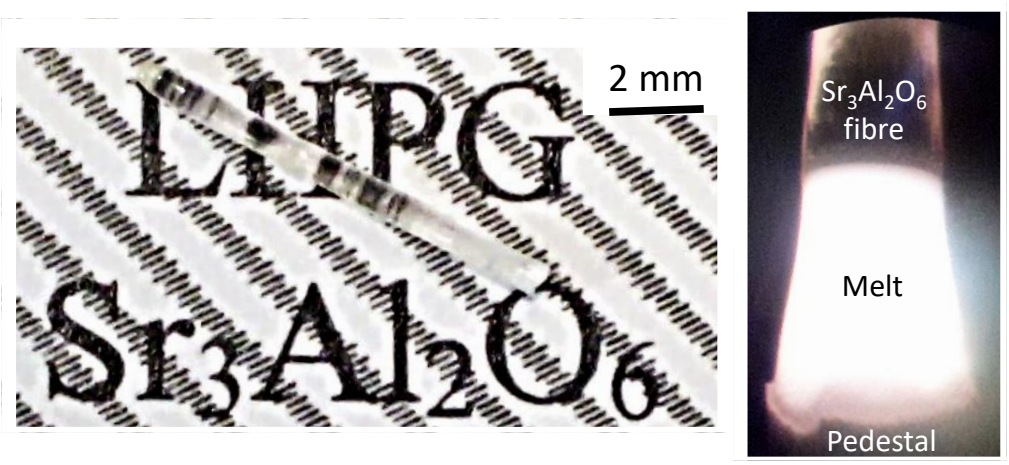

Figure 1: Photographs of the as-grown $Sr_3Al_2O_6$ fiber and the LHPG process.

The initial structural characterization has been performed using X-ray diffraction on both powdered source rod and crystalline fiber sample grown by LHPG technique. The XRD patterns are shown in Figure 2. The source rod XRD pattern exhibits well-defined sharp peaks pointing to a homogeneous sample with high crystallinity. According to X-ray powder diffraction data the pedestal and fiber samples match well with the $Sr_3Al_2O_6$ cubic structure (SG $Pa\bar{3}$, a = 15.844 Å). The main observed and calculated XRD reflections are shown in

Figure 2 (JCPDS 007-5481). One can notice some extra peaks in the LHPG fiber XRD pattern (the stars ✱ show the position of extra peaks) corresponding to monoclinic $Sr_{10}Al_6O_{19}$ secondary phase (S.G. *C*2/*c*, JCPDS 010-5791). Rietveld refinement was employed to estimate the percentage of this impurity which is about 2.7 vol%. We believe that the formation of this phase is related to some Al_2O_3 volatilization during the fiber drawing process. A similar phenomenon has been observed in Al_2O_3 micropulling down by Ghezal et al.[18] This hypothesis is supported by the fact that the raw rod materials can be crystallized as a $Sr_3Al_2O_6$ single phase upon heating at 1100 °C for 6 hours in conventional furnace (Figure S2).

Although the average crystal structures of $Sr_3Al_2O_6$ and $Sr_{10}Al_6O_{19}$ present different symmetry, both can be described in terms of perovskite-based superstructures (Figure 2c-d).[19, 20] On the one hand, $Sr_3Al_2O_6$ exhibits Al_6O_{18} puckered rings (Figure 2e) and possesses six inequivalent Sr sites which can be split in two Sr-sublattices. One of them is formed by three strontium ions six-fold coordinated by oxygen ions (Sr-O bond distances around 2.5 Å, forming irregular octahedra), and together with the two inequivalent aluminium sites, they form the framework related to perovskite materials (Figure 2c). The other three Sr ions form the second Sr sublattice. These ions are hosted within the voids between the polyhedra and also possess distorted environments, although their coordination number vary between nine, eight and seven (Sr-O bond lengths cover a wider range, between 2.43-2.93 Å).[19] On the other hand, $Sr_{10}Al_6O_{19}$ features the existence of $[Al_6O_{19}]^{20-}$ unbranched hexamers rather puckered (Figure 2f), in addition to eleven inequivalent Sr sites. Two of them are six-fold coordinated by oxygen forming irregular octahedra (Sr-O bond distances range between 2.35-2.52 Å) and together with the $[Al_6O_{19}]^{20-}$ hexamers form the underlying perovskite structure through corner shared SrO_6 and AlO_4 units. As in the case of $Sr_3Al_2O_6$, the remaining strontium cations are located within the voids and feature rather irregular coordination environments (they are eight to nine coordinated, and the Sr-O bond lengths vary between ~2.3-3.3 Å).[20] Overall, both compounds

present two kind of Sr, the ones building up the underlying perovskite structure (i.e. six coordinated), while other Sr ions are placed within the voids exhibiting much more distorted surroundings.

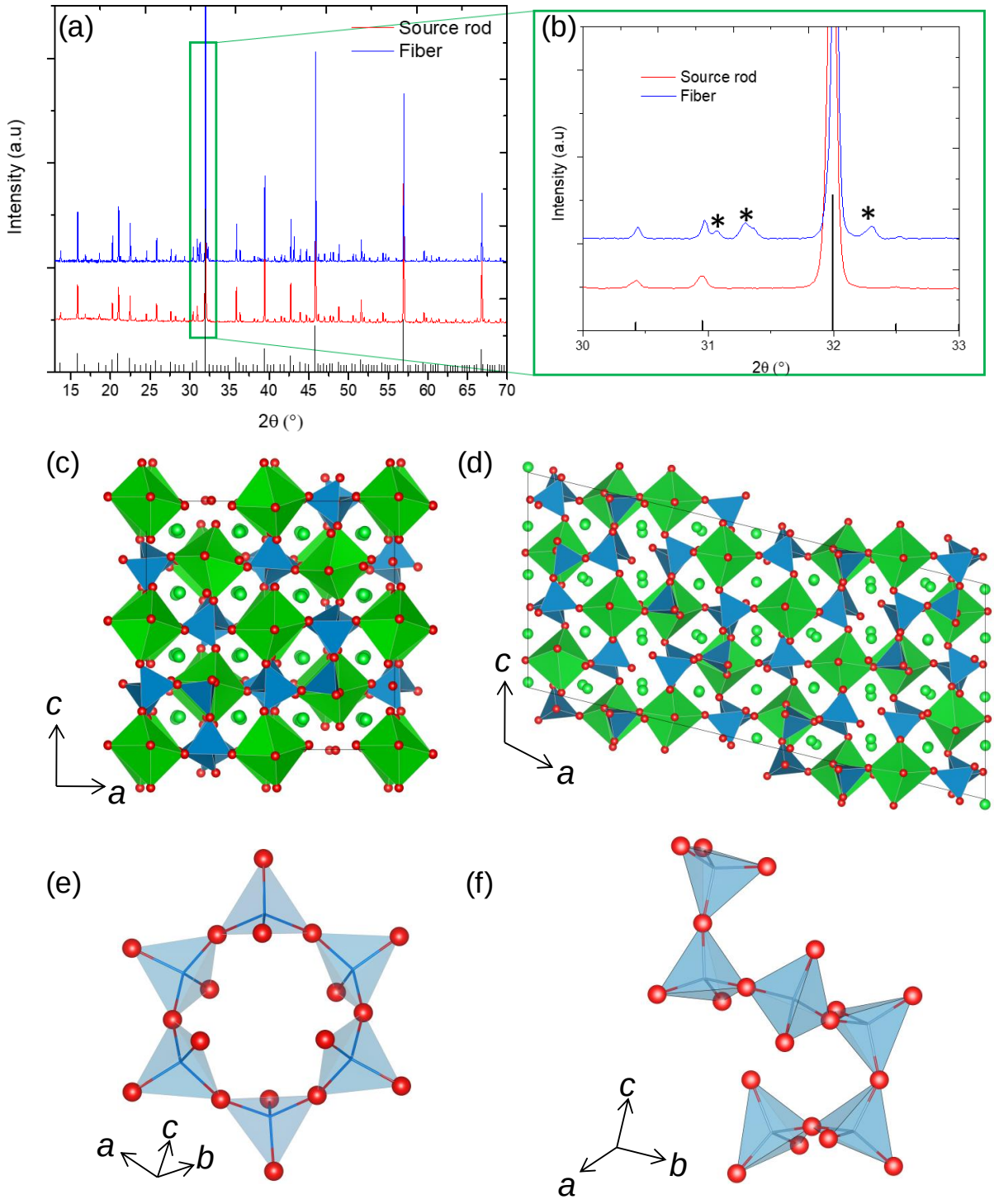

Figure 2: (a-b) XRD patterns of the pedestal (extruded rods) and as-grown LHPG fiber. Asterisks indicate extra reflection due to the existence of $Sr_{10}Al_6O_{19}$ secondary phase (2.7

wt%). [010] projections of the $Sr_3Al_2O_6$ (c) and $Sr_{10}Al_6O_{19}$ compounds (d). (e) View of the Al_6O_{18} ring. characteristic of $Sr_3Al_2O_6$ (f) View of the $[Al_6O_{19}]^{20-}$ hexamers presented in $Sr_{10}Al_6O_{19}$. The blue tetrahedra and the green octahedra represent AlO_4 and SrO_6 units. Red and green balls denote oxygen and Sr atoms, respectively.

3.2 Chemical composition and fiber microstructure

In all the as-grown $Sr_3Al_2O_6$ fibers prepared while varying the pulling conditions, SEM micrographs clearly reveal some bright elongated parts looking like "veins" running along the pulling direction inside a darker matrix as shown in Figure 3. The veins are depleted in Al while the Sr content is kept constant in both the veins and the matrix. Such unconventional microstructure has already been observed in $Bi_2ZnB_2O_7$ fibers grown by the micro-pulling down and LHPG technique. In this latter case, the origin of this peculiar feature was attributed to the evaporation of a substantial amount of boron oxide from the melt that locally changes the chemical composition in the ternary system and leads to incongruent melting behavior.[11] This further supports our previous hypothesis about the formation of $Sr_{10}Al_6O_{19}$ through Al_2O_3 evaporation during the drawing process assisted by laser heating. Indeed, according to X-Ray spectral analysis (EDS-SEM) and elemental maps, the chemical composition of the veins and the matrix slightly differs: a Sr/Al ratio of 1.50 (perfectly matching the $Sr_3Al_2O_6$ composition) and Sr/Al=1.62 are found for the matrix and the vein, respectively. The latter ratio is totally compatible with the presence of some $Sr_{10}Al_6O_{19}$ secondary phase (veins) within the $Sr_3Al_2O_6$ matrix, as evidenced by XRD on a crushed fiber.

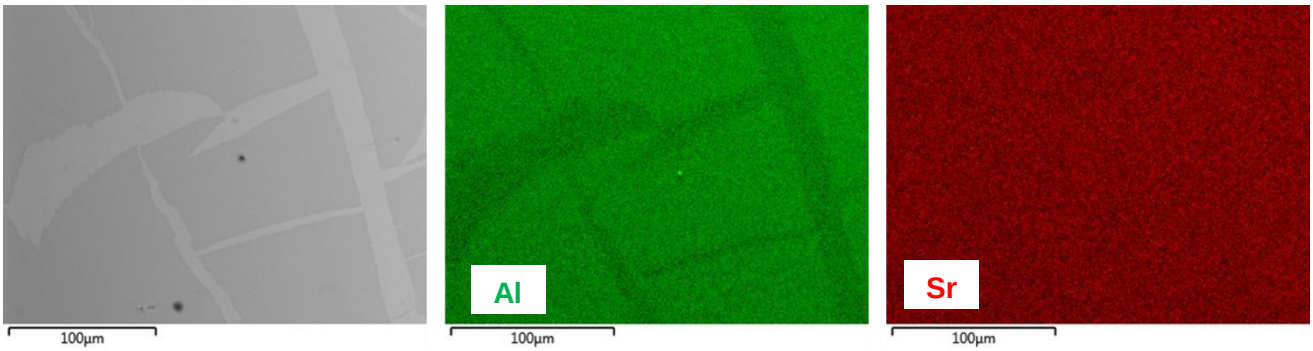

Figure 3: EDS-SEM elemental maps of the LHPG as-grown fiber

In order to find out the effect of the pulling process over the crystal growth, i.e. crystal orientation(s), EBSD data were acquired. The analysis revealed a complex multi-scale microstructure of the LHPG fibers. While the matrix exhibits a unique crystallographic orientation, the elongated veins parallel to the pulling direction are made of several domains with different crystallographic $Sr_3Al_2O_6$ orientations as shown in Figure 4a-4d. Even if the microstructures of the fibers grown from glass and crystalline seeds exhibit similar features, there exists a major proportion of veins, being more branched, for the former case (around 12±3% and 19±3 vol.%) which result in shorter fibers. Figure 4e shows the superimposition of two crystal indexations: $Sr_3Al_2O_6$ in red and $Sr_{10}Al_6O_{19}$ in green color. From the Image J image treatment software, the $Sr_{10}Al_6O_{19}$ crystalline fraction in the fiber is estimated at 3%. This value is close from the 2.7 vol% found from the XRD Rietveld refinement. The microstructure of the ceramic bulk is depicted in Figure 4e. The ceramic is mostly made of small polycrystalline grains with an average size around 3 µm.

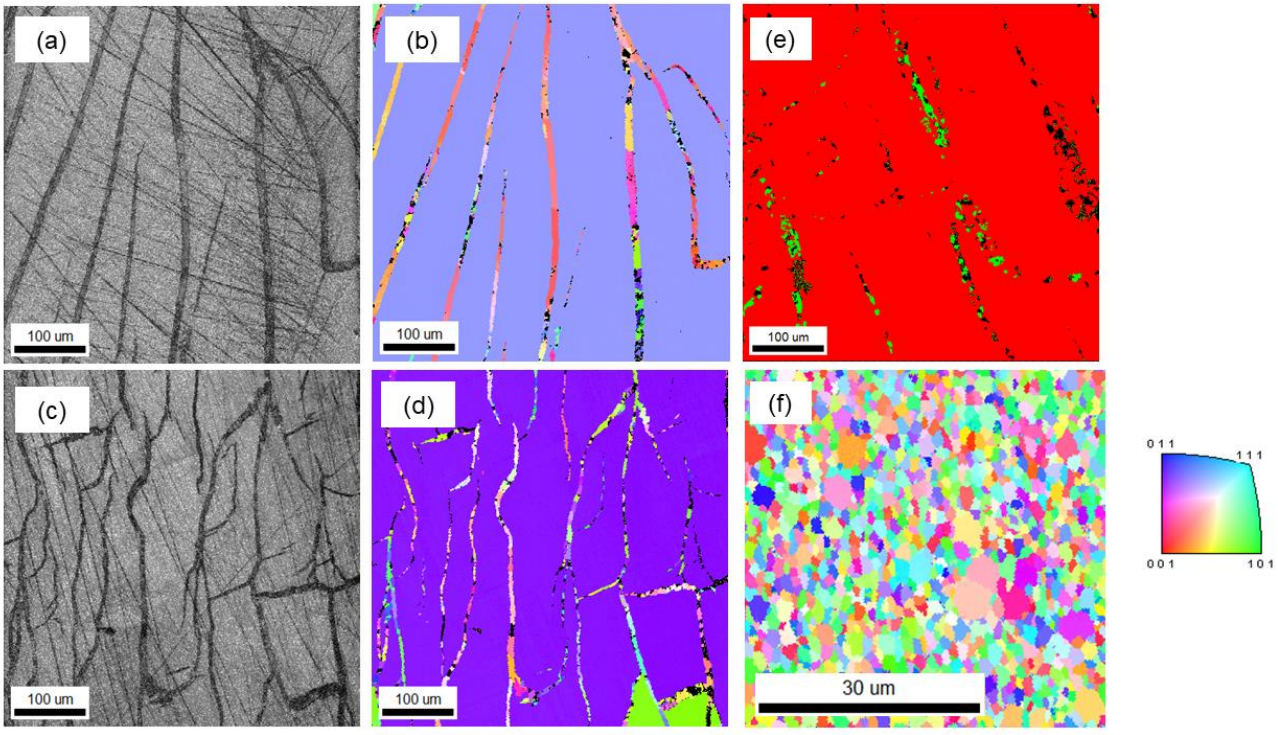

Figure 4: BSE-SEM images and corresponding EBSD maps of polished as-grown LHPG fiber (observation in the longitudinal direction) (a) (b) fiber grown from the glass seed with $Sr_3Al_2O_6$ indexation, (c) (d) fiber grown from the ceramic seed with $Sr_3Al_2O_6$ indexation, (e) fiber grown from the ceramic seed with $Sr_3Al_2O_6$ indexation (red color) and with $Sr_{10}Al_6O_{19}$ indexation (green color) (f) EBSD map of transparent ceramic bulk

To further understand the fiber local structure, Raman spectroscopy was used. Classic spectra and mappings were acquired. The 300-550 cm^{-1} wavenumber range can be associated to the bending mode Al-O-Al, O-Al-O as the 700-920 cm^{-1} wavenumber range can be correlated to the stretching Al-O mode. Compared to the matrix spectrum, some extra Raman bands or shoulders are observed in the vein at 515 cm^{-1} ($\nu_1[AlO_4^{5-}]$) and 756 cm^{-1} ($\nu_3[AlO_4^{5-}]$) (see black arrows in Figure 5).[21] The Raman bands of the veins fit perfectly the $Sr_3Al_2O_6$ cubic phase as shown in Figure 5 except for two bands. We can thus assume that these bands could be assigned to the terminal AlO_4 units present in the $Sr_{10}Al_6O_{19}$ composition identified as impurity by XRD and also evidenced by EBSD experiment in the "veins". As the mode at 756 cm^{-1} is more intense, this wavenumber range has been used for the study by principal component analysis.

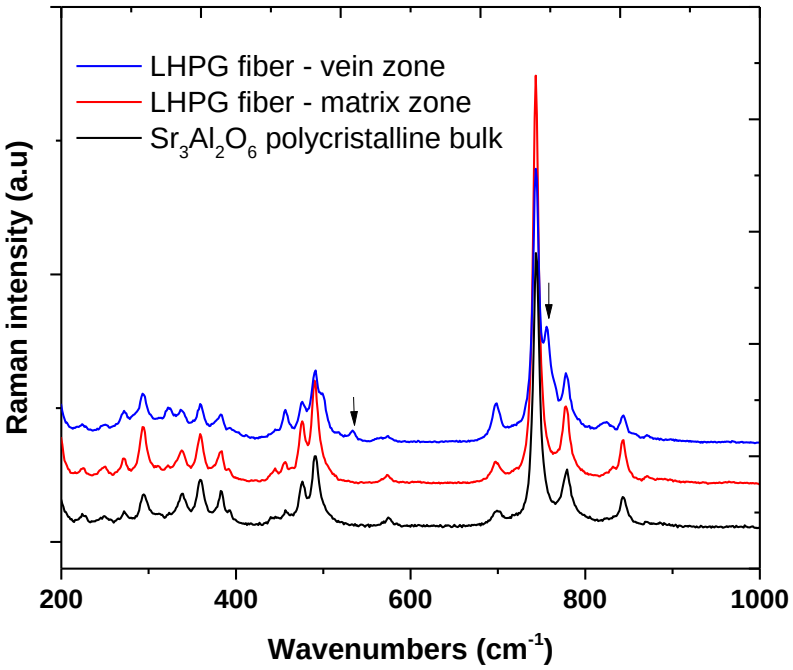

Figure 5: Raman spectra of the LHP fiber (vein and matrix) and the $Sr_3Al_2O_6$ polycristalline bulk for comparison

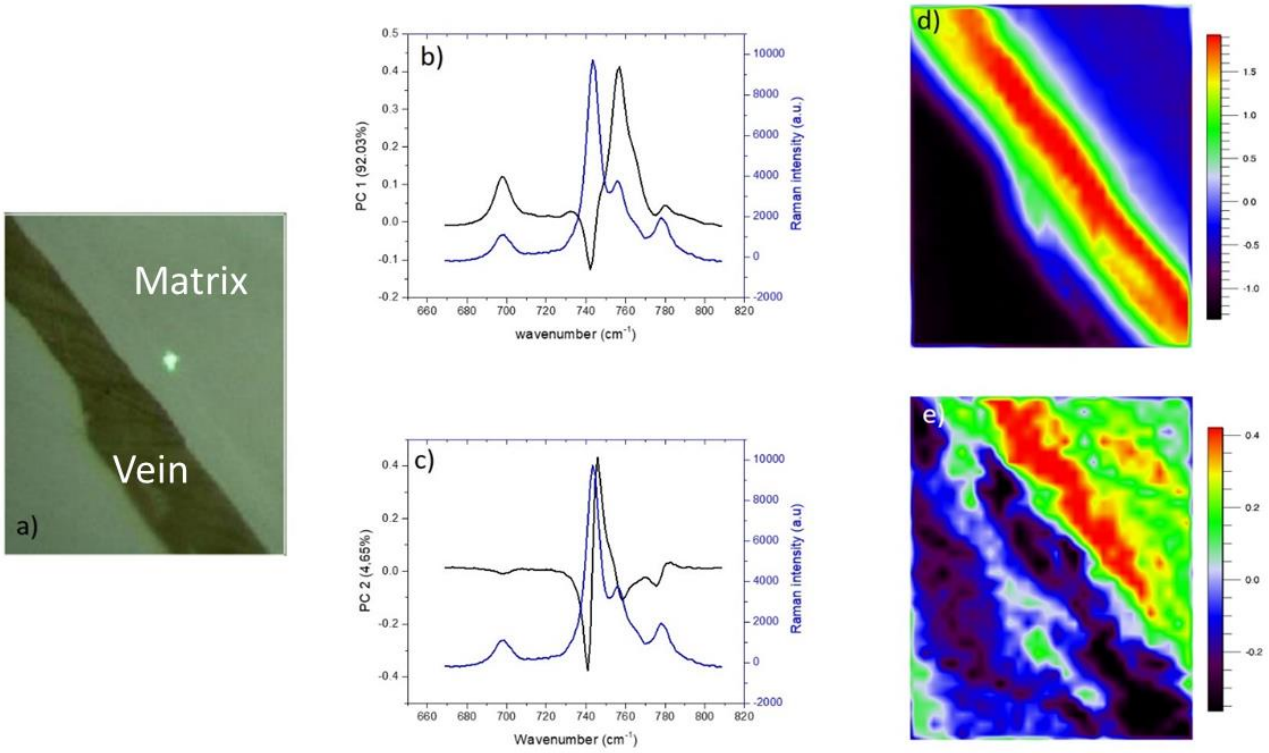

Figure 6: a) Optical view of the LHPG fiber mapped, b) principal component 1 and Raman spectrum of the vein as eye guide, c) component 2and Raman spectrum of the vein as eye guide, d) 2D Raman maps of the LHPG fiber reconstructed on PC1 e) 2D Raman maps of the LHPG fiber reconstructed on PC2.

As it can be seen on Figure 6b the first component (PC1) is mainly affected by the intensity of the mode localised at 756 cm^{-1}, as the second component (PC2) (Figure 6c) is mainly affected by the frequencies change of the 740 cm^{-1} vibrational mode. In this way, the Raman map reconstructed on the PC1 clearly localised the $Sr_{10}Al_6O_{19}$ phase within the vein as it is underlined by the color contrast of the map. PC2 points out the modification of the frequency of the main mode link to the stretching mode Al-O within the aluminium polyhedra of the $Sr_3Al_2O_6$ phase. The Raman map clearly localized this local stress at the vicinity of the vein (interface vein/matrix). We can suppose that this local constraint is probably due to the fibering process which is very severe with extremely large temperature gradients at the solid-liquid boundary during growth.

The interface vein/matrix was inspected by HRTEM (Figure 6). At low magnification, we see large lines oriented along the grain elongation axis and therefore potentially along the drawing axis. The orientation is always the same but we can see on the associated Fast Fourier Transform (FFT) pattern stretched diffraction spots which indicate some stacking structural defects. We can also observe the formation of rather narrow columnar domains due to the elongation of the fiber. This columnar structure with a very narrow dimension in thickness compared to the length may induce the stretched electron diffraction spots. At high resolution, the domains are slightly disoriented with each other although the general orientation remains the same. The vein is made up of a multitude of nanograins (Ø ≈ 5nm) in a little residual amorphous matrix. In HR-TEM, we can observe the cubic structure while in STEM-HAADF one can discern two types of sites. The brightest ones form large hexagons occupied only by Sr

atoms (green), while the darker sites are made up of a mixture of Sr / Al (purples) atoms and is less dense. In addition, the FFT pattern corresponding to the vein shows diffraction rings which are signing the presence of crystalline nanoparticles.

The elemental compositions of the grain and veins have also been determined by STEM-EDS analyses (Figure 6). A Sr/Al ratio of 1.45 and Sr/Al=1.55 are found for the matrix and the vein, respectively, which agree with the presence of $Sr_3Al_2O_6$ and $Sr_{10}Al_6O_{19}$, respectively. Finally, some precipitates enriched in Sr and Er that cross upper $Sr_3Al_2O_6$ grain and the vein are observed (green circle Figure 6a)

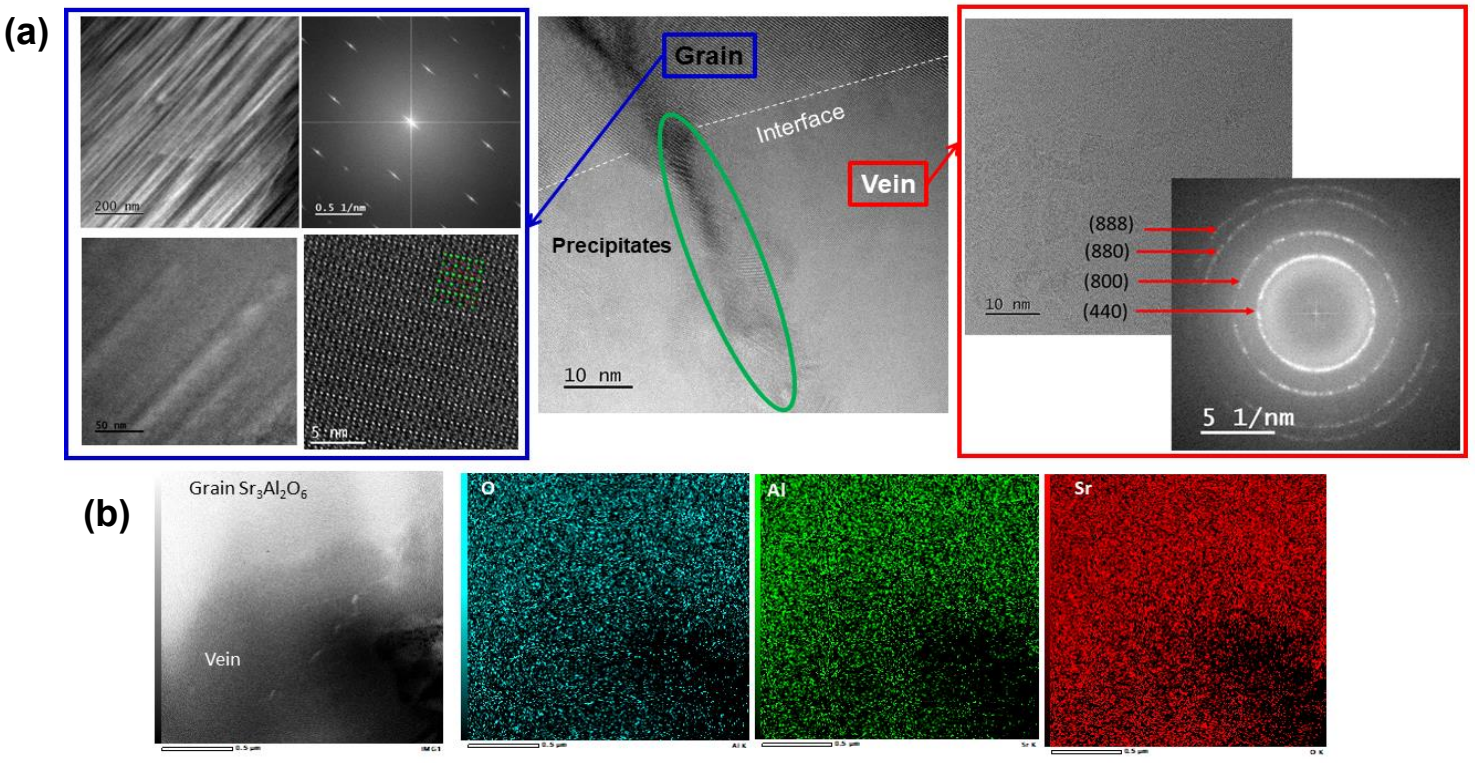

Figure 6: (a) HRTEM and (b) STEM-EDS observation of an interface grain/vein

3.3 Optical properties

Photoluminescence (PL) properties of 1 at% Er^{3+}-doped samples (bulks and fibers) were measured. We have focused our attention on the $^4I_{13/2} - {}^4I_{15/2}$ electronic transition and compared

the emission spectra for two LHPG fibers grown from ceramic and glass seeds to the PL emission spectrum collected in the case of a "reference" bulk transparent polycrystalline ceramic (Cf. Figure 7a). On one hand, one can first notice the strong similarities between all the spectra, simply suggesting similar crystal field effects due to similar environments of Er^{3+}. In addition, it is worth underlining that all the emission spectra recorded for our samples compare well to the ones reported by Singh *et al.* for Er^{3+}-doped and Er^{3+}/Yb^{3+}-codoped $Sr_3Al_2O_6$ samples.[15] On the other hand, one could also point out the discrepancies in the relative intensity, as well as the minor spectral differences. Indeed, the various Stark splitting are better defined in the case of the fibers compared to the "equivalent" bulk ceramic, thus clearly reflecting the superior and excellent crystalline quality of the grown materials, as already testified by the XRD data and HRTEM observations. Such moderate discrepancies probably originate from the fact that, whether Er^{3+} ions populate $Sr_3Al_2O_6$ or $Sr_{10}Al_6O_{19}$ phases, they are still positioned at the Sr sites (Al sites being far too small to accommodate rare earth ions). Although there exist several Sr sites (six inequivalent sites for $Sr_3Al_2O_6$ and eleven for $Sr_{10}Al_6O_{19}$), these environments are similar in both structures, as aforementioned. Furthermore, the PL decay curves data (see below) did not reveal any evidence for the existence of two different lifetime values which would reflect two different environments for Er^{3+} ions.

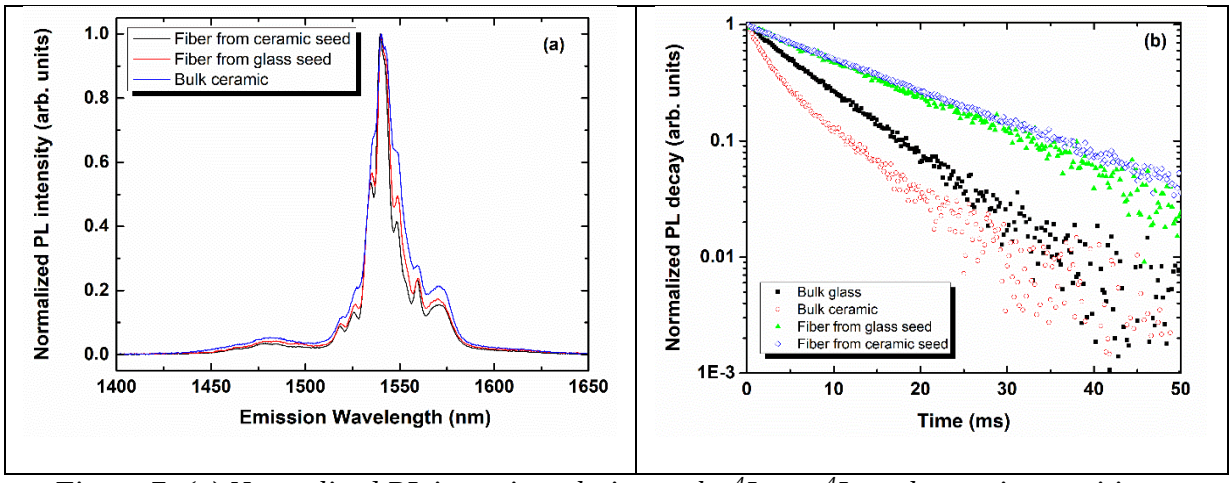

Figure 7: (a) Normalized PL intensity relative to the $^4I_{13/2} - {}^4I_{15/2}$ electronic transition: comparison of the data collected for the grown fibers with the data acquired for a

"reference" bulk polycrystalline ceramic (λ_{exc} = 377 nm). PL emission of the bulk glass (in comparison with the data of the bulk ceramic), as well as all the excitation spectra, are provided in the supplementary information. (b) Normalized PL decays measured for the two grown fibers, the bulk ceramic, as well as the glass sample.

Normalized PL decay curves relative to the $^4I_{13/2} - {}^4I_{15/2}$ electronic transition are plotted in Figure 7b. The PL decay curves collected for both LHPG fibers and bulk-glass exhibit almost a unique lifetime value. Effectively, normalized PL decay curves plotted in semi-logarithmic scale can be almost perfectly fitted using a straight line, with a quality factor depicted by the r^2 value equal at least to 0.997. Thus, for LHPG fibers, macroscopic PL decay measurements clearly did not reveal any evidence for an additional lifetime value that would be characteristic of Er^{3+} ions localized in different environments (for instance, Er^{3+} ions present within the veins, in Sr-rich precipitates and/or in the multitude of the nanograins and/or in the residual amorphous matrix – Cf. HRTEM observations).

In addition, it is noteworthy that the PL decay curve relative to the bulk transparent ceramic sample (Figure 7b) is the only one which does not correspond to a straight line. In that case, two different exponential decay functions will be necessary in order to correctly fit the experimental data (a longer lifetime value, $\tau_1 \sim 7.60 \pm 0.05$ ms, and another one much shorter, $\tau_2 \sim 1.75 \pm 0.05$ ms). The first lifetime value is very similar to the one encountered for the bulk glass sample (7.80 ± 0.05 ms – see Table 1): it reflects the presence of Er^{3+} ions perfectly dispersed within the ceramic grains. The second lifetime value is by far shorter, and reflects segregation/clustering effects that will occur while transforming the parent glass into a fully crystallized transparent ceramic. In optical ceramics, depending on its chemical nature, it is indeed known that segregation of the rare earth ions might occur at grain boundaries and/or that dopant concentration might vary from one grain to another.[22] Thus, some moderate segregation

of the Er^{3+} ions is likely at play during the full congruent crystallization process, whereas such effects are not at all evidenced for LHPG fibers.

Considering that the bulk ceramic sample behaves differently than the others (two lifetimes *vs* a unique one), in order to be able to compare all the samples together, we have calculated the average lifetime values $< \tau >$ using the following equation:

$$< \tau > = \frac{\int_0^t I(t).t.dt}{\int_0^t I(t).dt}$$

All the extracted data are gathered in Table 1, and one can notice the consequent reduction (~ -20 %) of the average lifetime value concomitant with the full congruent crystallization process (from 7.80 to 6.25 ms).

Table 1. Fluorescence average lifetime values of the initial $^4I_{13/2}$ level for the four samples analyzed in this work. For the bulk ceramic sample, the two different lifetime values extracted from the use of two exponential decay functions in order to fit the experimental data.

	Fiber from ceramic seed	**Fiber from glass seed**	**Bulk transparent ceramic**	**Bulk glass**
Fluorescence lifetime (ms) of the initial $^4I_{13/2}$ level	13.60 ± 0.10	12.75 ± 0.10	6.25 ± 0.05 (unique average value) 7.60 ± 0.05 / 1.75 ± 0.05 Long / Shorter lifetimes	7.80 ± 0.05

Finally, what must be primarily highlighted is the exceptional long fluorescence lifetime values (up to more than 13.5 ms) measured for the $^4I_{13/2}$ excited state in the case of LHPG fibers, in comparison with some literature data for equivalent or similar doping concentrations: 6.83 ms for $Sr_3Al_2O_6$,[15] 8 ms for $SrGdGa_3O_7$ single-crystal[23] 6.5 ms for YAG crystals,[5] just below 7 ms for Er^{3+}:YAG single-crystal fibers also grown by LHPG, 4.3 ms for $LiNbO_3$ bulk material[24] and 5.75 ms for Er^{3+}-doped $Y_3Ga_5O_{12}$ nano-garnets.[25] For LHPG fibers, the lifetime value was more than doubled in comparison with the average lifetime value $< \tau >$ measured for the bulk

ceramic sample (6.25 ms); the latter value being rather comparable to that of 6.83 ms reported in .[15] Again, this reflects the excellent crystalline quality evidenced by HRTEM observations, and definitely constitutes serious potentialities of the grown LHPG fibers for laser applications.

Ultimately, when comparing both spectral and lifetime data, it clearly appears that the performances of our LHPG fibers are rather comparable, whatever the nature (glass or ceramic) of the seed. Nevertheless, the use of the different seed nature should be tempered. The employ of crystalline seed leads to longer fibers and better crystalline quality that slightly extent the Er^{3+} emission lifetime. Nevertheless, the employ of a $Sr_3Al_2O_6$ glass seed could be an attractive alternative to simplify the overall processing of the fibers, even though our experiments indicate a larger propagation of veins resulting in shorter fibers.

4. Conclusion

$Sr_3Al_2O_6$ transparent optical fibers were successfully prepared by LHPG technique. The microstructure of the fiber is rather complex and features, in the main, a single orientated $Sr_3Al_2O_6$ bulk together with polycrystalline veins with $Sr_{10}Al_6O_{19}$ composition. Either glass and polycrystalline $Sr_3Al_2O_6$ seeds were employed, although a large proportion of veins were observed when the glass seed was used which hinder the drawing process. The same technique turned out to be very useful for the synthesis of 1 at% Er^{3+}-doped $Sr_3Al_2O_6$ and the resulting fibers exhibit an intense luminescence characterized by a relatively long lifetime (13.5+/- 0.1 ms) when comparing to other Er^{3+}-doped materials. The transparency as well as the photoluminescent properties of Er^{3+}-doped $Sr_3Al_2O_6$ fiber suggest it to be an excellent candidate material for optical applications.

Acknowledgements

A.J. Fernandez-Carrion gratefully acknowledges an COST Action MP1401 grant (COST-STSM-ECOST-STSM-MP1401-050617-088753).

References

1. Wang, W. L.; Wang, J. S.; Huang, Y. C.; Liu, L. W.; Huang, S. L.; Cheng, W. H. Few-Mode Cr-Doped Crystalline Core Fibers for Fiber Amplifier. *IEEE Photonics Technology Letters* **2012,** 24, 1628-1631.
2. Feigelson, R. S. Pulling optical fibers. *Journal of Crystal Growth* **1986,** 79, 669-680.
3. Yoon, D.-H.; Yonenaga, I.; Fukuda, T.; Ohnishi, N. Crystal growth of dislocation-free $LiNbO_3$ single crystals by micro pulling down method. *Journal of Crystal Growth* **1994,** 142, 339-343.
4. Yoshikawa, A.; Nikl, M.; Boulon, G.; Fukuda, T. Challenge and study for developing of novel single crystalline optical materials using micro-pulling-down method. *Optical Materials* **2007,** 30, 6-10.
5. Andreeta, M. R. B.; Hernandes, A. C. In *Springer Handbook of Crystal Growth*; Dhanaraj, G., Byrappa, K., Prasad, V., Dudley, M., Ed.; Springer Berlin Heidelberg: Berlin, Heidelberg, 2010; pp 393-432.
6. Nie, C. D.; Bera, S.; Harrington, J. A. Growth of single-crystal YAG fiber optics. *Optics Express* **2016,** 24, 15522-15527.
7. Shi, P. C. W.; Watson, I. A.; Sharp, J. H. High-concentration Er:YAG single-crystal fibers grown by laser-heated pedestal growth technique. *Optics Letters* **2011,** 36, 2182-2184.
8. Nubling, R. K.; Harrington, J. A. Single-crystal laser-heated pedestal-growth sapphire fibers for Er:YAG laser power delivery. *Applied Optics* **1998,** 37, 4777-4781.
9. Jundt, D. H.; Fejer, M. M.; Byer, R. L. Characterization of single‐crystal sapphire fibers for optical power delivery systems. *Applied Physics Letters* **1989,** 55, 2170-2172.
10. Rey-García, F.; Costa, F. M.; Zaldo, C. Laser floating zone growth of Yb, or Nd, doped (Lu0.3Gd0.7)2SiO5 oxyorthosilicate single-crystal rods with efficient laser performance. *Journal of Materials Chemistry C* **2020,** 8, 2065-2073.
11. Assi, F.; Ferriol, M.; Cochez, M.; Aillerie, M.; Ponting, B.; Maxwell, G. Towards good quality $Bi_2ZnB_2O_7$ fibers grown by the micro-pulling down technique. *Journal of Crystal Growth* **2016,** 451, 1-5.
12. Alimov, O.; Dobretsova, E.; Guryev, D.; Kashin, V.; Kiriukhina, G.; Kutovoi, S.; Rusanov, S.; Simonov, S.; Tsvetkov, V.; Vlasov, V.; Voronov, V.; Yakubovich, O. Growth and Characterization of Neodymium-Doped Yttrium Scandate Crystal Fiber with a Bixbyite-type Crystal Structure. *Crystal Growth & Design* **2020,** 20, 4593-4599.
13. Bera, S.; Ohodnicki, P.; Collins, K.; Fortner, M.; Picard, Y. N.; Liu, B.; Buric, M. Dopant segregation in YAG single crystal fibers grown by the laser heated pedestal growth technique. *Journal of Crystal Growth* **2020,** 547, 125801.
14. Alahraché, S.; Al Saghir, K.; Chenu, S.; Véron, E.; De Sousa Meneses, D.; Becerro, A. I.; Ocaña, M.; Moretti, F.; Patton, G.; Dujardin, C.; Cussó, F.; Guin, J.-P.; Nivard, M.; Sangleboeuf, J.-C.; Matzen,

G.; Allix, M. Perfectly Transparent $Sr_3Al_2O_6$ Polycrystalline Ceramic Elaborated from Glass Crystallization. *Chemistry of Materials* **2013,** 25, 4017-4024.

15. Singh, V.; Seshadri, M.; Singh, N.; Mohapatra, M. Radiative properties of Er^{3+} doped and Er^{3+}/Yb^{3+} co-doped $Sr_3Al_2O_6$ phosphors: exploring the usefulness as a phosphor material. *Journal of Materials Science: Materials in Electronics* **2019,** 30, 2927-2934.

16. Al Saghir, K. Céramiques transparentes par cristallisation complète du verre : application aux aluminosilicates de strontium. 2014.

17. Reyes Ardila, D.; Andreeta, M. R. B.; Cuffini, S. L.; Hernandes, A. C.; Andreeta, J. P.; Mascarenhas, Y. P. Single-crystal $SrTiO_3$ fiber grown by laser heated pedestal growth method: influence of ceramic feed rod preparation in fiber quality. *Materials Research* **1998,** 1, 11-17.

18. Ghezal, E. A.; Li, H.; Nehari, A.; Alombert-Goget, G.; Brenier, A.; Lebbou, K.; Joubert, M. F.; Soltani, M. T. Effect of Pulling Rate on Bubbles Distribution in Sapphire Crystals Grown by the Micropulling Down (μ-PD) Technique. *Crystal Growth & Design* **2012,** 12, 4098-4103.

19. Alonso, J. A.; Rasines, I.; Soubeyroux, J. L. Tristrontium dialuminum hexaoxide: an intricate superstructure of perovskite. *Inorganic Chemistry* **1990,** 29, 4768-4771.

20. Kahlenberg, V. Synthesis and crystal structure of $Sr_{10}Al_6O_{19}$: a derivative of the perovskite structure type in the system $SrO–Al_2O_3$. *Materials Research Bulletin* **2002,** 37, 715-726.

21. Black, L.; Breen, C.; Yarwood, J.; Deng, C. S.; Phipps, J.; Maitland, G. Hydration of tricalcium aluminate (C3A) in the presence and absence of gypsum—studied by Raman spectroscopy and X-ray diffraction. *Journal of Materials Chemistry* **2006,** 16, 1263-1272.

22. Zhao, W.; Anghel, S.; Mancini, C.; Amans, D.; Boulon, G.; Epicier, T.; Shi, Y.; Feng, X. Q.; Pan, Y. B.; Chani, V.; Yoshikawa, A. Ce^{3+} dopant segregation in $Y_3Al_5O_{12}$ optical ceramics. *Optical Materials* **2011,** 33, 684-687.

23. Piao, R.-Q.; Wang, Y.; Zhang, Z.-B.; Zhang, C.-Y.; Yang, X.-F.; Zhang, D.-L. Optical and Judd-Ofelt spectroscopic study of Er^{3+}-doped strontium gadolinium gallium garnet single-crystal. **2019,** 102, 873-878.

24. Chi-Hung, H.; McCaughan, L.; Gill, D. M. Evaluation of absorption and emission cross sections of Er-doped $LiNbO_3$ for application to integrated optic amplifiers. *Journal of Lightwave Technology* **1994,** 12, 803-809.

25. Venkatramu, V.; León-Luis, S. F.; Rodríguez-Mendoza, U. R.; Monteseguro, V.; Manjón, F. J.; Lozano-Gorrín, A. D.; Valiente, R.; Navarro-Urrios, D.; Jayasankar, C. K.; Muñoz, A.; Lavín, V. Synthesis, structure and luminescence of Er^{3+}-doped $Y_3Ga_5O_{12}$ nano-garnets. *Journal of Materials Chemistry* **2012,** 22, 13788-13799.